PROCEEDINGS A

rspa.royalsocietypublishing.org

Research

Article submitted to journal

Subject Areas:
Fluid mechanics

Keywords:
fluid, body, interaction, channel, modelling, analysis

Author for correspondence:
Frank T Smith
e-mail: f.smith@ucl.ac.uk

Movement of a finite body in channel flow

Frank T Smith and Edward R Johnson

Department of Mathematics, UCL, Gower Street, London, WC1E 6BT

A body of finite size is moving freely inside, and interacting with, a channel flow. The description of this unsteady interaction for a comparatively dense thin body moving slowly relative to flow at medium-to-high Reynolds number shows that an inviscid core problem with vorticity determines much, but not all, of the dominant response. It is found that the lift induced on a body of length comparable with the channel width leads to differences in flow direction upstream and downstream on the body scale which are smoothed out axially over a longer viscous length scale; the latter directly affects the change in flow directions. The change is such that in any symmetric incident flow the ratio of slopes is found to be $\cos(\pi/7)$, i.e. approximately 0.900969, independently of Reynolds number, wall shear stresses and velocity profile. The two axial scales determine the evolution of the body and the flow, always yielding instability. This unusual evolution and linear or nonlinear instability mechanism arise outside the conventional range of flow instability and are influenced substantially by the lateral positioning, length and axial velocity of the body.

1. Introduction

This study is on the movement of a body within a viscous fluid flow inside a channel, with the body motion and the fluid motion interacting with each other. We are concerned with understanding and predicting the interactive behaviour from basic dynamics for a single body of finite size. The theory takes a two-dimensional setting and starts with the assumption of a solid body of length comparable with the channel width, free to travel inside the very long channel, asking the question of how it and the fluid flow evolve in time.

THE ROYAL SOCIETY PUBLISHING

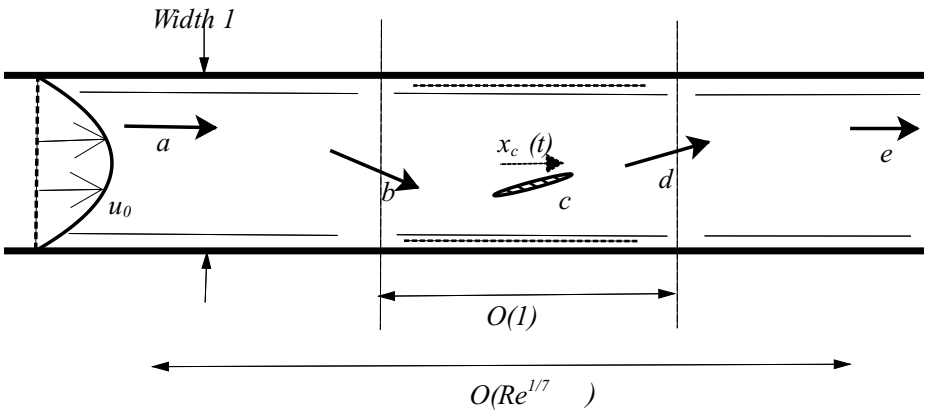

Figure 1. Unsteady fluid-body interplay as thin body moves freely in channel flow: non-dimensional sketch, not to scale. Oncoming velocity profile u_0 has no slip at the walls. Typical flow direction $abcde$ shown has zero incidence at a, e, nonzero at b, d, and is along the body at c; the ratio of slopes at b, d is found in § 4. Axially the body velocity is $x_c(t)$ and the main length scales are of orders 1, $Re^{1/7}$. Two wall layers are induced on the former scale but only one on the latter, as shown.

Numerous applications motivate the work. In a biomedical context the interest lies in the transport of drugs, thrombi or obstructions along blood vessels or through vessel networks and similarly in the lung airways [1–4]. On industrial applications, the travel of ice shards and other solid objects into engine intakes or out of exhausts [5–7], the travel of food grains along sorting chutes [8], and similar situations, motivate the study of fluid-body interaction. These include the transport of rubble down chutes, plumbing problems and dust movement inside hoovers as well as sedimentation, light particles or seeds in particle velocimetry, cleaning and washing processes. There are many different scales here. The emphasis throughout is on high flow rates corresponding to high Reynolds numbers. Apart from studies at low flow rates [9–11] previous work in the area is based mostly on direct numerical simulations and few experiments [12–16]. There are recent studies of a more analytical nature on full interactions between the fluid and the body or multiple bodies [8,17,18] but these are dominated largely by inviscid reasoning with attached or turbulent boundary layers being assumed *ab initio*. Little or no other work on a self-consistent basis accounting for the influences of viscous-inviscid effects appears to have been published on full fluid-body interaction with rational contributions in the laminar viscous layers. Moreover, given that the length scales of small bodies or particles which are of much practical concern frequently lie outside the conventional range for fluid flow instability and transition there is interest in whether linear or nonlinear growth and /or instability can arise when a two-way interplay between fluid and body is present. This interest is supported somewhat by recent direct numerical simulations [19] on delays in relaminarisation of transitional-turbulent channel flow.

The present focus is on linear and nonlinear interactions at medium-to-high Reynolds numbers in which the body and fluid motions affect each other at leading order. The theory incorporates different incident forms of the internal fluid flow ahead of the finite body, with no slip at the walls. Parametric understanding is key overall. Delicate issues surround the channel-flow evolution here as well as subsequent questions on where a body ends up when travelling in a vessel network and the influence of a chain of bodies travelling in sequence which develop sheltering in their wakes. Many issues remain to be clarified; a reasonable start on tackling them is to take the representative velocity of the body to be relatively small compared with the fluid velocity. The following sections on the fluid-body interaction for unsteady laminar planar incompressible-fluid flow consider the body motion and the fluid-flow pressure and velocities in the vessel as time progresses: see figure 1. § 2 describes the physics, scales and governing equations for the

body-scale parts of the interaction, covering the core and wall-layer responses, the body motion and most importantly the far field of the body scale where the flow directions deviate from those very far upstream. These deviations are responsible for a nontrivial viscous-inviscid interplay that arises over the two major axial scales. §3 shows that only a *relative* core problem remains inviscid at leading order, whereas the full-core problem is fixed by longer-scale viscous effects as addressed in §4. §5 provides a closer inspection of the body-scale properties. Wall pressure and wall shear stress (WSS) contributions at the outer walls are included. Further discussion is presented in §6 while an appendix considers the response as the body velocity is increased successively with relation to the local viscous-layer fluid velocity.

2. The fluid-body interaction

The fluid flow and body motion evolve inside an almost straight channel. A non-dimensionalisation is made in which fluid-flow velocities are measured relative to the typical axial velocity u_D in the channel, lengths are measured with respect to the channel width a_D and the Reynolds number Re is $u_D a_D/\nu_D$ where ν_D is the kinematic viscosity of the fluid. A subscript D denotes a dimensional quantity. The pressure is based on $\rho_D u_D^2$, with ρ_D being the fluid density, and time is based on a_D/u_D. The body is closed and of uniform density ρ_{BD}, mass M_D and moment of inertia I_D per unit distance perpendicular to the plane of the motion. In non-dimensional terms therefore the channel width is unity, the body length is L say, the planar Cartesian coordinates are x, y, sometimes referred to below as horizontal and vertical as in figure 1, the corresponding flow velocity components are u, v, the pressure is p, while t denotes the time. The characteristic axial flow velocity is of order unity.

Sufficiently far upstream of the body the incident flow is unidirectional with profiles $u_0(y), \psi_0(y)$ for the velocity and stream function (here $u_0(y) = \psi_0'(y)$) which are of general $O(1)$ form with a positive velocity except at the outer walls, with a normalised wall shear stress $u_0'(0) = \lambda^-$ of order unity at the lower wall and similarly at the upper wall $u_0'(1) = -\lambda^+$ say. Here Re is large. The Froude number is also large. Along with the above incident motion there is a corresponding pressure gradient $\mathrm{d}p/\mathrm{d}x$ of order $1/Re$. The body length is now taken to be of order unity. Orders of magnitude as in [20,21] then indicate that the flow structure comprises mainly a core of quasi-inviscid flow, viscous outer-wall layers near $y = 0, 1$ and two viscous layers on the body itself. The core gives all but one of the dominant features and is described in detail next.

The scales, the core flow and the body motion. The present configuration has a thin moving body nearly aligned with the containing channel walls, as in figure 1, and in effect both the upper and the lower surfaces of the body lie at an $O(1)$ height $y = y_0$ say inside the channel. Hence the typical normal displacement h and typical angle θ on the body are small. The axial length scale L of the body being comparable with the channel width implies that we focus first on x of $O(1)$ and so within the majority of the surrounding fluid motion there is significant normal variation in the pressure as well as across the body itself. Also the viscous outer-wall layers remain thin compared with the channel width. From an inertial-viscous balance of momentum these layers have thickness $O(Re^{-1/3})$ locally, although supplemented by over-riding slightly thicker but still thin layers due to longer viscous scales, and so the major part or core of the flow where y is of order unity is expected to be quasi-inviscid. This indicates the order of magnitude of the disturbance in the core if fluid-body interaction is to take place. Thus for

$$x = O(1), \tag{2.1}$$

the flow solution expands in the form

$$[u, \psi, p] = [u_0, \psi_0, 0] + Re^{-m}\,[u_E, \psi_E, 0] + Re^{-N}\,[u_1(x, y, T), \psi_1(x, y, T), p_1(x, y, T)] + \ldots \tag{2.2}$$

for y of $O(1)$ in the core. Here ψ is the stream function associated with u, v. The effects u_E, ψ_E are due to longer-scale displacements which are pressure-free and independent of x: thus $0 <$

$m < N$ and $u_E = A_0 u_0'(y), \psi_E = A_0 u_0(y)$. The relevant powers m, N and function $A_0(T)$ are to be determined. In contrast the unknown perturbations u_1, ψ_1, p_1 are functions of x, y, T to be found locally, subject to the perturbations having to match with the incident flow properties. A comparatively slow axial movement of the body is incorporated by means of a constant velocity $c_{\rm body} \ll 1$ and the coordinate system is taken to move with that velocity, so that in effect the channel walls are moving slowly upstream. The constant $c_{\rm body}$ is discussed further in Appendix A. The time is scaled as $t = \gamma_1 T$ where γ_1 is assumed to be suitably large. Substitution into the Navier-Stokes equations then yields a quasi-steady response in which to leading order $u_1 = \partial\psi_1/\partial y, v_1 = -\partial\psi_1/\partial x$ and the continuity and x-, y-momentum equations yield the steady linearised Euler system provided that γ_1 exceeds $O(1)$. Hence the governing equation of the core is

$$u_0(y)\nabla^2\psi_1 = u_0''(y)\psi_1. \tag{2.3a}$$

This is subject to the conditions of tangential flow on approach to the walls and of matching in the far-field,

$$\psi_1 = 0 \text{ at } y = 0, 1, \tag{2.3b}$$

$$\psi_1 \text{ does not grow exponentially as } x \to \pm\infty, \tag{2.3c}$$

respectively, as well as tangential flow near the enclosed body. The pressure perturbation is then given explicitly by

$$p_1(x, y, T) = p_{1\infty} + u_0'(y)\psi_1 - u_0(y)\psi_{1y}, \tag{2.3d}$$

where the constant $p_{1\infty}$ is the scaled pressure upstream and downstream over the length scale (2.1). In general the core flow produces zero pressure variation $p_1 - p_{1\infty}$ at the walls as u_0, ψ_1 are zero there but a nonzero unknown slip velocity $u_1 = \lambda^{\pm} A^{\pm}(x, T)$ say is produced at the upper $(+)$ and lower $(-)$ walls in turn.

The enclosed moving body of finite length occupying $0 \leqslant x \leqslant L$ has thickness and orientation which are compatible with the disturbances in (2.2). The nonzero velocity u_0 at height y_0 implies that the zero-normal-flow condition applies on the unknown moving-body surface which is written as

$$y = y_0 + Re^{-N} f^{\pm}(x, T) \ \ [0 < x < L]. \tag{2.4}$$

The fluid flow is separation-free and so the Blasius-like viscous layers on the upper and lower body surfaces remain negligibly thin [21]. In consequence of the above and the time scale the kinematic boundary condition becomes

$$\psi_1^{\pm} = u_0(y_0)(-f^{\pm} + K^{\pm}) \text{ at } y = y_0^{\pm} \ \ [0 < x < L], \tag{2.5}$$

where $K^{\pm}(T)$ are unknown constants at any specific time. Here the upper $(+)$ and lower $(-)$ surface shapes in (2.4) are given more explicitly by

$$f^{\pm}(x, T) = \hat{h}(T) + (x - L/2)\hat{\theta}(T) + \hat{c}(x) \pm \hat{t}(x)/2 \ \ [0 < x < L]\,. \tag{2.6}$$

The known functions $\hat{c}(X), \hat{t}(X)$ denote respectively the scaled camber and thickness of the given body shape whereas the variables $\hat{h}, \hat{\theta}$ acting over the time scale T denote respectively the unknown normal displacement of the centre of mass of the body and the unknown angle of the centreline of the body as it moves. Both $\hat{h}, \hat{\theta}$ are based on the scale Re^{-N} relative to h, θ because of (2.4). They vary in time according to the Newtonian balances of normal momentum and angular momentum, namely

$$\hat{M} d^2\hat{h}/dT^2 = C_L, \text{ with } C_L = \int_0^L \{p_1(x, y_0-, T) - p_1(x, y_0+, T)\}\, \mathrm{d}x, \tag{2.7a}$$

$$\hat{I} d^2\hat{\theta}/dT^2 = C_M, \text{ with } C_M = \int_0^L (x - L/2)\{p_1(x, y_0-, T) - p_1(x, y_0+, T)\}\, \mathrm{d}x, \tag{2.7b}$$

at leading order. The unknowns $C_L(T), C_M(T)$ are respectively the scaled evolving lift and moment coefficients, while $\hat{M}, \hat{I}$ are defined by $Re^N M_D/(a_D^2 \rho_D \gamma_1^2), Re^N I_D/(a_D^4 \rho_D \gamma_1^2)$ where

the dimensional mass M_D and moment of inertia I_D of the body are themselves comparable with $Re^{-N}a_D^2\rho_{BD}, Re^{-N}a_D^4\rho_{BD}$ in turn. Thus the time scale is such that

$$\gamma_1 = O\left((\rho_{BD}/\rho_D)^{\frac{1}{2}}\right) \tag{2.7c}$$

and so the ratio of body density over fluid density must be large here. We suppose $\hat{M}, \hat{I}$ are of the same order throughout. The centre of mass is at the symmetry location $x = L/2$ since the body has uniform density, while the body's orientation with θ being small implies that the pressures p_1 at $y = y_0\pm$ are exerted vertically to leading order on either surface of the body. The pressures are the dominant forces from the fluid flow. In contrast the balance of horizontal or axial momentum gives simply $\hat{M}d^2x_C/dT^2 = 0$ for the horizontal movement of the scaled centre-of-mass position x_C, since the horizontally resolved effects from the flow pressure and surface shear stress are relatively small, and so the velocity $\mathrm{d}x_C/\mathrm{d}T$ is constant; this is in keeping with the smallness of c_{body} described in the previous paragraph.

The wall layers. The viscous wall layers near $y = 0, 1$ will require consideration since they affect the induced wall shear stresses and pressures. Their influences on the body movement are found to be secondary however, and so detailed discussion of them is deferred to §4. We note here the estimates

$$O(Re^{-1/3}), O(Re^{-N}), O(Re^{-1/3-N}) \tag{2.8}$$

for the thicknesses, the velocity disturbances and the pressure variations inside the upper and lower wall layers based on (2.2)-(2.3d) and on orders of magnitude. The pressure variations are much less than in the core.

Other contributions. The final pieces of the interactive structure occur close to the leading edge $X = 0$ and upstream and downstream of the body. First, a tiny zone of extent $O(Re^{-N})$ at most which is of Navier-Stokes or Euler type is produced near the leading edge. The type depends on the particular local shape of the thin body in general but in the present cases the evolution with time puts the emphasis on flat plates, for which the former type applies. The global effects from this zone are negligible. Second, ψ_1 must be continuous everywhere on the body in (2.5) and continuous at $X = 0+$. This leads to the relation

$$\hat{K}^+ = \hat{K}^- = K, \tag{2.9a}$$

say. The presence of $K(T)$ arises in a sense from properties at the trailing edge $X = 1$ where a Kutta-like condition applies in order to keep the flow separation-free and continuity of pressure holds across the wake, requiring

$$p_1(1, y_0-, T) = p_1(1, y_0+, T) \text{ for all } T. \tag{2.9b}$$

The flux required by $K(T)$ in (2.9a) based on the stream function has to adjust or be adjusted to ensure that (2.9b) is satisfied, a requirement which accentuates the spatial ellipticity of the flow-body interaction at each time level. Third, significant upstream and downstream influence occurs over a longer length scale $O(Re^{1/7})$ (see [22,23] and figure 1) as described later.

The far field of the core. The constraints upstream and downstream in (2.3c) require specifically that

$$\psi_1 \sim (A_u - \beta_u x)u_0(y) \text{ as } x \to -\infty, \psi_1 \sim (A_d - \beta_d x)u_0(y) \text{ as } x \to +\infty, \tag{2.10a}$$

where $A_u, \beta_u, A_d, \beta_d$ are unknown functions of time. The right-hand sides in (2.10a) are exact solutions of the governing equation (2.3a) giving nonparallel flow directions or nonzero streamline slopes. The suggestion of nonzero streamline slope β_u, β_d emerging upstream and /or downstream is perhaps surprising. It agrees however with an integral of the governing equation (2.3a) over the flow domain which enables the differences in streamline slope to be related to the

scaled lift, giving

$$\beta_u - \beta_d = C_L/J, \text{ with } J = \int_0^1 u_0^2(y)dy, \tag{2.10b}$$

from the divergence theorem. The growing displacement effects proportional to β_u, β_d on the present length scale (2.1) are smoothed out over the longer length scale studied in § 4. The prime system appears to be (2.3a, b, d) with (2.5)-(2.7b) and (2.9a)-(2.10b) for the evolving core flow and body motion but this is subject to considerable adjustments below.

3. Core flow solutions in their relative form

The time dependence. A central problem is that of zero thickness $\hat{t}$ and zero camber $\hat{c}$. The reason for addressing it lies in the finding of exact linear and nonlinear solutions for the fluid-body interactions with only height $\hat{h}$ and angle $\hat{\theta}$ present. The complete solution of the evolutionary system can then be expressed in terms of exponential responses in time T such that

$$\left[\psi_1, p_1, f^{\pm}, \hat{h}, \hat{\theta}, K, \beta_d \ldots\right] = \sum_Q \left[\psi_{11}(x,y), p_{11}(x,y), f_{11}^{\pm}(x), h_{11}, \theta_{11}, K_{11}, \beta_{11d} \ldots\right] e^{QT} \tag{3.1}$$

takes effect. The admissible values of the real or complex constant factor Q are to be found. The system remains as before in the new variables but with (2.7a,c) replaced by

$$\hat{M}Q^2 h_{11} = C_{11L}, \hat{I}Q^2\theta_{11} = C_{11M}, \tag{3.2a}$$

respectively. The values of $\hat{h}, \hat{\theta}$ are set by the original initial conditions at time T zero. Now effectively $p_{1\infty}, \hat{c}, \hat{t}$ are zero and in addition the new system is as if steady.

Normalised relative-core problem. To identify the core contribution we write

$$\psi_{11} = (A_{11u} - \beta_{11u}x)u_0(y) + \psi_{12}, p_{11} = p_{12}. \tag{3.3}$$

We also put $H_{12} = h_{11} - \beta_{11u}L/2 + A_{11u}, \phi_{12} = \theta_{11} - \beta_{11u}$ as the relative heights and slopes, to obtain the very same system except that (2.5)-(2.6) and (2.10a) are replaced by

$$\psi_{12}^{\pm} = u_0(y_0)(K_{12} - H_{12} - (x - L/2)\phi_{12}) \text{ at } y = y_0^{\pm}\,[0 < x < L]\,, \tag{3.4a}$$

$$\text{and } \psi_{12} \to 0 \text{ as } x \to -\infty, \psi_{12} \sim (A_{12d} - A_{12u} + [\beta_{12u} - \beta_{12d}]\,x)u_0(y) \text{ as } x \to +\infty, \tag{3.4b}$$

in turn. The dependence on the difference in slopes $(\theta_{11} - \beta_{11u})$ makes physical sense. A normalisation is applied next to account for the influence of ϕ_{12}, namely

$$[\psi_{12}, p_{12}, K_{12}, H_{12}, \phi_{12}, \beta_{12d}, \ldots] = \phi_{12}\left[\psi^*, p^*, K^*, H^*, 1, \beta_d^*, \ldots\right]. \tag{3.5}$$

The relative problem becomes, as a 'First Step', a purely fluid-dynamical one in normalised form:

$$u_0(y)\nabla^2\psi^* = u_0''(y)\psi^*. \tag{3.6a}$$

$$\psi^* = 0 \text{ at } y = 0, 1, \tag{3.6b}$$

$$p^*(x,y) = u_0'(y)\psi^* - u_0(y)\psi_y^*, \tag{3.6c}$$

$$\psi^{*\pm} = u_0(y_0)(K_H - (x - L/2)) \text{ at } y = y_0 \pm\,[0 < x < L]\,, \tag{3.6d}$$

$$p^*(L, y_0-) = p^*(L, y_0+). \tag{3.6e}$$

$$\psi^* \to 0 \text{ as } x \to -\infty, \qquad \partial\psi^*/\partial x \to D_s u_0(y) \text{ as } x \to +\infty, \tag{3.6f}$$

$$D_s = C_L^*/J, \text{ with } C_L^* = \int_0^L \{p^*(x, y_0-) - p^*(x, y_0+)\}\,\mathrm{d}x. \tag{3.6g}$$

Here the closed inviscid problem (3.6a-g) is found to fix the slope-difference $D_s = [\beta_u^* - \beta_d^*]$ as well as $K_H = K^* - H^*$ (even though the individual slopes β_d^*, β_u^* themselves remain undetermined: they are fixed by longer-scale effects of § 4, representing the 'Second Step'). Solutions have been obtained numerically and analytically as follows.

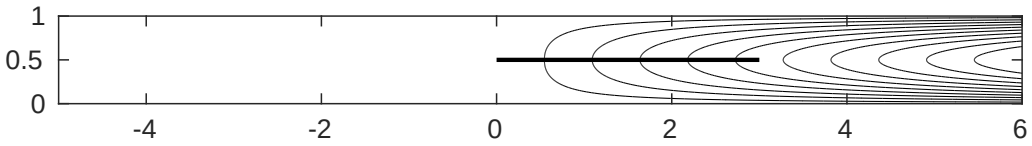

Figure 2. Streamline perturbations for relative-core problem for Poiseuille flow. Here $L = 3$ and $y_0 = 0.5$.

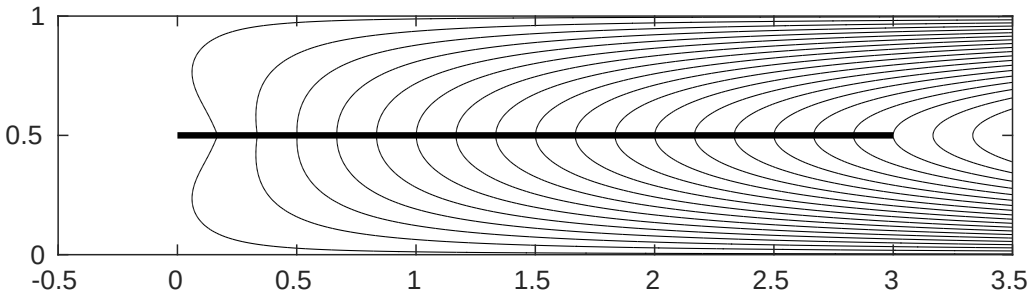

Figure 3. A detail of figure 2

Solutions. Numerical solutions were obtained for the basic example of the velocity profile

$$u_0 = y - y^2 \tag{3.7}$$

of plane Poiseuille flow by means of a finite-difference procedure. The infinite channel is truncated to a finite length in X and approximated, including boundary points, by a uniform mesh of $N = n_x \times n_y$ points. The field equation (3.6*a*) is approximated at interior points by standard central differencing and Dirichlet conditions (3.6*b*), (3.6*d*) add further linear equations at the corresponding boundary points, with K_H becoming an additional unknown. Normal derivatives at boundaries are approximated by three-point one-sided derivatives and thus (3.6*c*), (3.6*e*) give an additional linear equation, determining K_H, while (3.6*f*) determines the downstream boundary values of ψ^* with D_s also becoming an unknown. Equation (3.6*g*) furnishes the additional equation to determine D_s, where the integral is evaluated along the plate away from the leading edge using the trapezium rule. The integral over the mesh interval on the plate commencing at the leading edge is evaluated analytically by taking the pressure to be proportional to $x^{-1/2}$ within the interval. It remains to treat the upstream boundary. All eigenfunctions of the unforced governing equations decay exponentially except $u_0(y)$ and $xu_0(y)$. The eigenfunction $xu_0(y)$ is eliminated by requiring that $\partial\psi^*/\partial x$ vanishes at the upstream boundary and the eigenfunction $u_0(y)$ is eliminated by further requiring that ψ^* is orthogonal to $u_0(y)$ there. The problem thus reduces to $N + 3$ linear equations in the $N + 2$ unknowns of the ψ^* mesh values and K_H and D_s. A least-squares solution of this system is found numerically directly using the MATLAB backslash operator for sparse matrices.

All results presented here (except those for $L = 0.1$) are for a computational grid with $-5 \leq x \leq 6$ and 2201×201 points, giving along-channel and cross-channel grid-spacings of $1/200$ and maximum error, over all grid points, in the linear equations of order 10^{-4}. Halving the grid spacing in each direction altered the solution by less than 10^{-4} (except for $L = 0.1$) as did doubling the length of the computational domain. For $L = 0.1$ the grid is 4401×401 to ensure that the pressure is sufficiently smooth along the plate to maintain an accuracy of 10^{-4}. Figure 2 shows perturbation streamlines in the whole computational domain for a plate of length $L = 3$ in the centre of the channel, $y_0 = 0.5$. The perturbations here and in figures 3 – 6 appear to intersect the

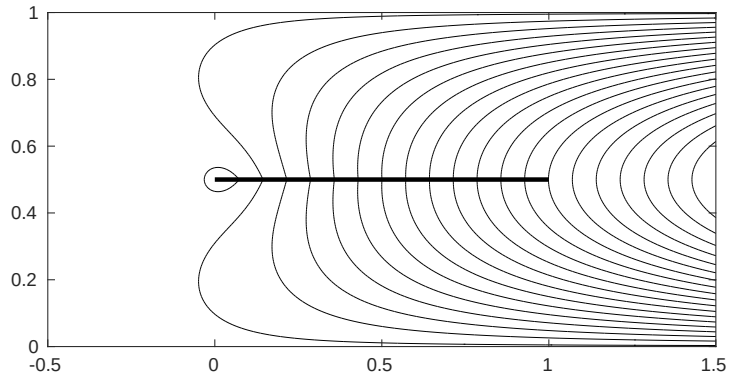

Figure 4. A plate at $y_0 = 0.5$ as in figure 3 but for $L = 1$.

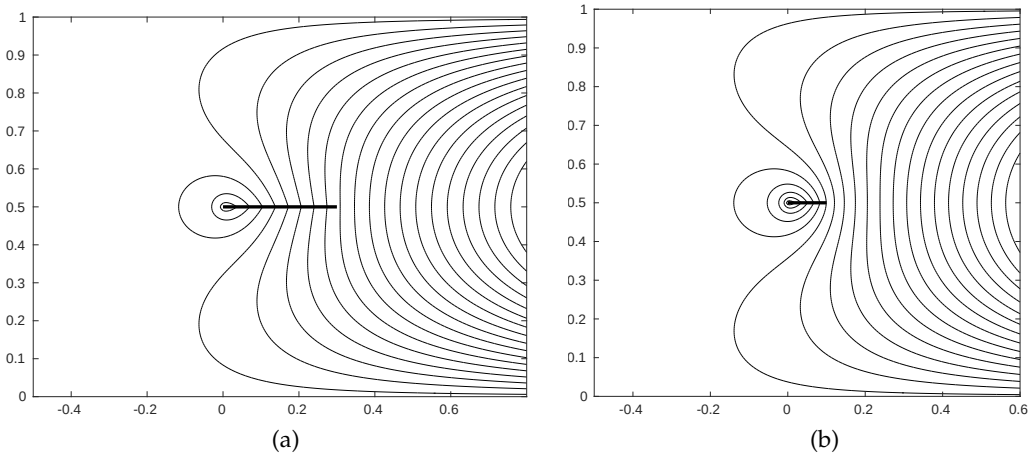

Figure 5. A plate at $y_0 = 0.5$ as in figures 3 and 4 but for (a) $L = 0.3$, (b) $L = 0.1$.

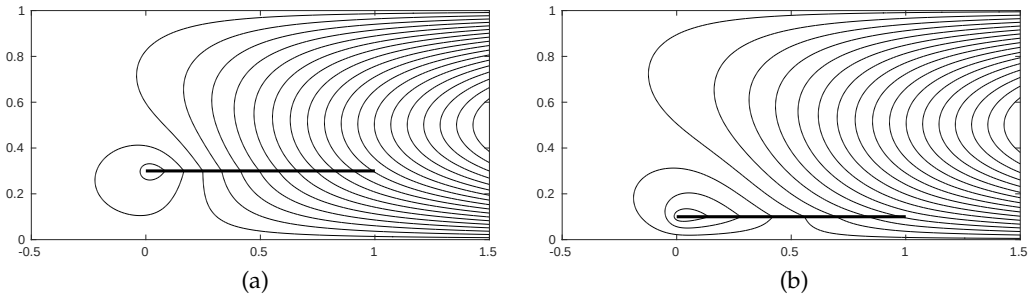

Figure 6. A plate of length $L = 1$ as in figure 4 but at (a) $y_0 = 0.3$, (b) $y_0 = 0.1$.

body simply because of the linearisation present in the core motion. Figure 3 shows perturbation streamlines for the flow near the plate for $L = 3$ and figures 4 and 5 show the changes in the flow for the progressively shorter bodies with $L = 1, 0.3$ and 0.1. Figure 3 and figure 6 show the changes in the flow for a unit length plate located progressively closer to the lower boundary, $y_0 = 0.5$, 0.3 and 0.1. Figures 7 and 8 show the corresponding pressure distributions on the plate and the tangential speed along the lower wall with parts (a) showing the effects of plate shortening and

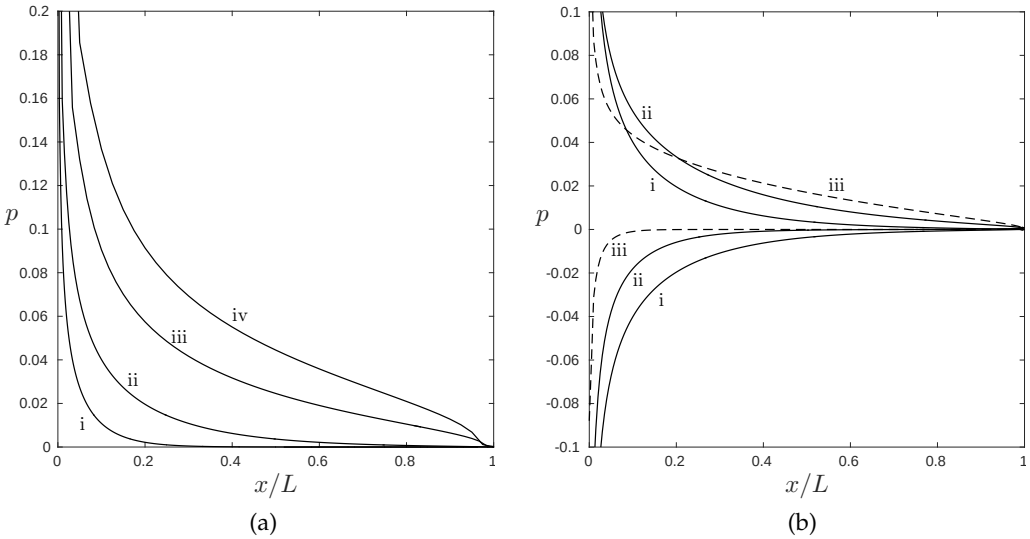

Figure 7. The pressure above and below the plate as a function of x/L. (a) For figures 3, 4 and 5 so $y_0 = 0.5$ and (i) $L = 3$, (ii) $L = 1$, (iii) $L = 0.3$, (iv) $L = 0.1$. Since the plate lies at the centre of the channel the pressure is odd across the plate and so plots of the pressure below the plate are omitted. (b) For figures 4 and 6 so $L = 1$ and (i) $y_0 = 0.5$, (ii) $y_0 = 0.3$, (iii) (dashed lines) $y_0 = 0.1$.

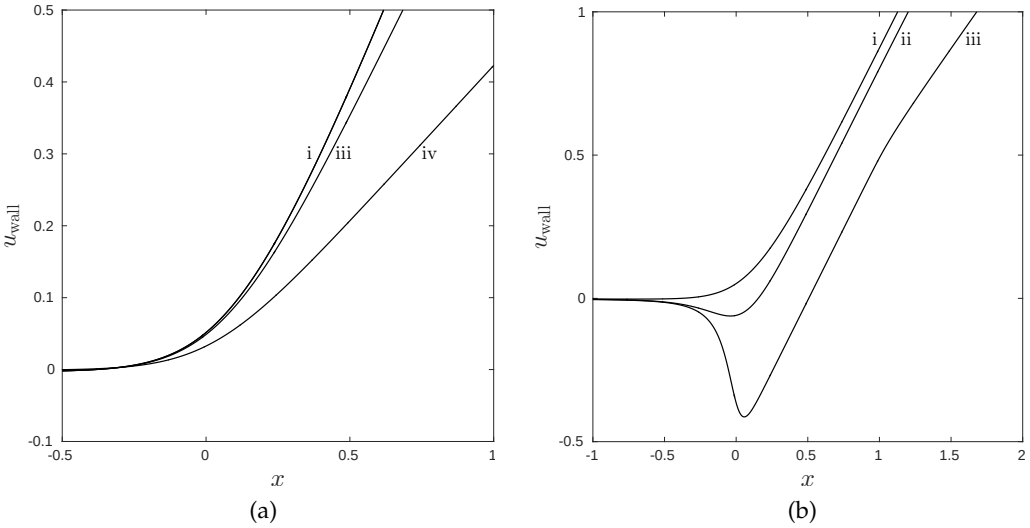

Figure 8. The tangential speed along the wall $y = 0$. (a) For figures 3, 4 and 5 so $y_0 = 0.5$ and (i) $L = 3$, (ii) $L = 1$, (iii) $L = 0.3$, (iv) $L = 0.1$. The curves for $L = 1$ and $L = 3$ are indistinguishable and thus the label (ii) is omitted. (b) For figures 4 and 6 so $L = 1$ and (i) $y_0 = 0.5$, (ii) $y_0 = 0.3$, (iii) $y_0 = 0.1$.

parts (b) showing the effects of a given plate approaching the wall. More physical insights into the results are given in subsequent sections.

Analytical solutions are obtainable for near-plug incident profiles such that

$$u_0 = 1 \text{ across the majority of the relative core,} \tag{3.8a}$$

supplemented by thin layers near the walls $y = 0, 1$ where the profile reduces to zero. The majority of the core is thus governed by Laplace's equation from (3.6a) with (3.8a) but the thin layers of

thickness $\delta \ll 1$ say play an important role as they lead to the boundary conditions becoming

$$\partial\psi^*/\partial y \to 0 \text{ as } y \to 0, 1. \tag{3.8b}$$

This non-standard form follows from the leading-order balance of (3.6a) in the lower thin layer becoming $u_0(y)\partial^2\psi^*/\partial y'^2 = u_0''(y')\psi^*$ since $y = \delta y'$ is small there, with the solution being $\psi^* = A_P(x)u_0(y')$. Here $A_P(x)$, which is the unknown $O(1)$ value of ψ^* at $y = 0+$ resulting from application of (3.8b), gives a relative slip velocity $\delta^{-1}A_P(x)\mathrm{d}u_0/\mathrm{d}y'(0)$ which is comparatively large. Similar reasoning holds in the upper thin layer and both layers are of thickness larger than that of the typical viscous wall layers. Solutions for the near-plug case follow from mapping techniques. In particular if the body is midway between the walls so that $y_0 = \frac{1}{2}$ a solution symmetric about the midway line can be sought with, at $y = \frac{1}{2}, \partial\psi^*/\partial y = 0$ for $x < 0, x > L$ but $\psi^* = (-x + \chi)$ for $0 < x < L$ from (3.6d). The constant $\chi = -(L/2 + K_H)$. We map the channel interior in terms of the complex coordinate $z = x + iy$ to an upper half-plane in $\bar{\bar{z}} = \bar{\bar{x}} + i\bar{\bar{y}}$ by the conformal transformation

$$\bar{\bar{z}} = \exp(2\pi z) \tag{3.9a}$$

which takes ∞ downstream to vertical ∞ in $\bar{\bar{z}}$ and ∞ upstream to the origin in $\bar{\bar{z}}$. We then work with u^*, v^* since the boundary conditions on the $\bar{\bar{x}}$-axis are $u^* = 0$ everywhere except in $\bar{\bar{x}}_1 < \bar{\bar{x}} < \bar{\bar{x}}_2$ wherein $v^* = 1$. Here $\bar{\bar{x}}_1 = -\exp(2\pi L)$, $\bar{\bar{x}}_2 = -1$ are both negative. So

$$u^* - iv^* = -i\Gamma(\bar{\bar{z}} - \bar{\bar{x}}_1)^{1/2}/(\bar{\bar{z}} - \bar{\bar{x}}_2)^{1/2} - i \tag{3.9b}$$

for some real constant Γ. Note that as $\bar{\bar{z}} \to 0$ we have $v^* \to \Gamma\exp(\pi L) + 1$. From (3.9a,b) along the symmetry line

$$\text{at } y = \frac{1}{2}: \qquad v^* - 1 = \begin{cases} \Gamma((e^{2\pi L} - e^{2\pi x})/(1 - e^{2\pi x}))^{1/2} & x < 0; \\ 0 & 0 < x < L; \\ \Gamma((e^{2\pi x} - e^{2\pi L})/(e^{2\pi x} - 1))^{1/2} & x > L. \end{cases} \tag{3.10a}$$

Making $v^* \to 0$ upstream thus gives $\Gamma = -\exp(-\pi L)$; hence then $v^* \to 1 - \exp(-\pi L)$ downstream; hence the result $C_L^* = (\exp(-\pi L) - 1)$ would be expected from (3.6g). Similarly we find

$$\text{at } y = \frac{1}{2}: \qquad u^* = \begin{cases} 0 & x < 0; \\ -\Gamma((e^{2\pi L} - e^{2\pi x})/(e^{2\pi x} - 1))^{1/2} & 0 < x < L; \\ 0 & x > L. \end{cases} \tag{3.10b}$$

Therefore the pressure on the underside of the body is (see figure 9)

$$\text{at } y = \frac{1}{2}-: \qquad p^* = \Gamma(e^{2\pi L} - e^{2\pi x})/(e^{2\pi x} - 1))^{1/2} \text{ for } 0 < x < L. \tag{3.10c}$$

So then the scaled lift on the body, taking into account antisymmetry of u, p about $y = \frac{1}{2}$, is (see figure 9)

$$C_L^* = 2\Gamma\int_0^L ((e^{2\pi L} - e^{2\pi x})/(e^{2\pi x} - 1))^{1/2}\,\mathrm{d}x = \exp(-\pi L) - 1, \tag{3.10d}$$

on integration. This agrees with the value anticipated just after (3.10a) and also with a direct numerical evaluation of (3.10d).

The body motion in the sense of Q in (3.2a, b) is determined by virtue of viscous effects in the next section. The added effects of nonzero thickness $\hat{t}$ and camber $\hat{c}$ are much less than those associated with the scaled height and angle whenever Q_r is positive, corresponding to significant temporal growth of these $(\hat{h}, \hat{\theta})$ compared with the steady thickness and camber $(\hat{t}, \hat{c})$.

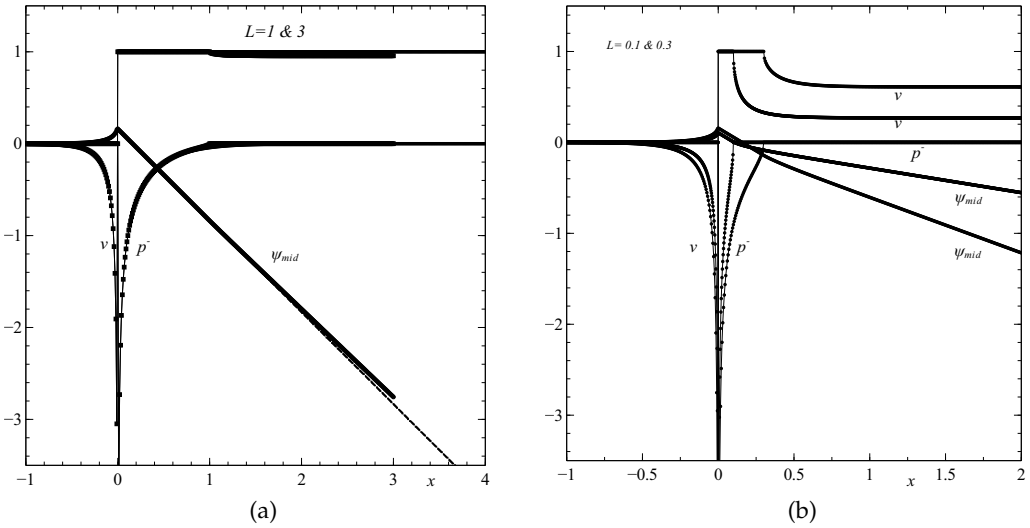

Figure 9. Core properties for plug-flow case. (a) $L = 1$, 3 (with $L = 1$ results curtailed at $x = 3$ to reveal $L = 3$ results more clearly). (b) $L = 0.1$, 0.3.

4. Viscous effects and the body motion

Over a longer viscous length scale. The 'Second Step', to complete the fluid-body-interaction solution and hence find the temporal power Q and streamline slope β_d^N, relies on viscous effects. These act mainly over a length scale

$$x = Re^{1/7}X, \text{ with } X \text{ of } O(1), \tag{4.1}$$

[22]. The expansion of the core flow then is

$$[u, \psi, p] = [u_0, \psi_0, 0] + Re^{-2/7}\left[\tilde{u}_1(X, y, T), \tilde{\psi}_1(X, y, T), \tilde{p}_1(X, y, T)\right] + \dots \tag{4.2a}$$

while in the wall layers where $y = Re^{-2/7}Y$ (lower layer) and $1 - Re^{-2/7}\tilde{Y}$ (upper layer)

$$[u, \psi, p] = [Re^{-2/7}U, Re^{-4/7}\Psi, Re^{-4/7}P^{\pm}] + \dots . \tag{4.2b}$$

The core solution is dominated by inviscid displacement effects but has $\partial\tilde{p}_1/\partial y$ being nonzero which yields a relationship between the scaled upper- and lower-wall pressures $P^{\pm}(X, T)$, namely

$$P^+ - P^- = JA_{XX}. \tag{4.3a}$$

(The definition of J is in (2.10c).) Those pressures in turn affect the viscous wall layers which have nonlinear governing equations; in the lower layer

$$U = \Psi_Y, V = -\Psi_X, UU_X + VU_Y = -P_X^- + U_{YY}. \tag{4.3b}$$

This is subject to the requirement of matching with (2.10a,b) at small $|X|$, together with

$$U = V = 0 \text{ at } Y = 0, \text{ and } U \sim \lambda(Y + A(X, T)) \text{ as } Y \to \infty, \tag{4.3c}$$

at all $O(1)X$ values for zero relative slip at the channel wall and for matching with the core solution respectively. For the balance in (4.3a) to hold the time scale $\gamma_1 \gg Re^{3/7}$ which exceeds $O(1)$ as assumed earlier: in fact coupling with (2.7e) indicates that the density ratio ρ_{BD}/ρ_D must exceed the order of $Re^{6/7}$. The upper viscous wall layer is similar, essentially having (4.3a-c) again but with $\psi = -Re^{-4/7}\tilde{\Psi}$ and $U \sim \lambda^+ Y - \lambda^+ A(X, T)$ as $Y \to \infty$, as well as P^+ instead of P^-, with $\tilde{Y}$ replacing Y. The unknown pressures $P^{\pm}$ and core displacement A here yield

viscous-inviscid interaction. The axial matching with the shorter-scale responses in the previous two sections imposes the local conditions

$$A \sim O(1) - \beta_{d,u} X \text{ as } X \to 0\pm \tag{4.4}$$

in view of (2.10a,b). This also serves to show that $m = 2/7, N = 3/7$ in (2.2) and that $A_0 = A(0,T)$.

To help understand the whole interaction more we consider small disturbances in which $A, P^{\pm}, f^{\pm}, \hat{h}, \hat{\theta}, K$ are of order ϵ where ϵ is a small amplitude parameter. Then the system of interest in the first step remains (3.6a-i) whereas the present second step involves the linearised relations

$$U^{\pm} = \Psi^{\pm}_Y, V^{\pm} = -\Psi^{\pm}_X, \lambda^{\pm} Y U^{\pm}_X + V^{\pm} \lambda^{\pm} = -P^{\pm}_X + U^{\pm}_{YY} \tag{4.5a}$$

from the upper and lower viscous wall layers subject to the requirements

$$U^{\pm} = V^{\pm} = 0 \text{ at } Y = 0, \text{ and } U^{\pm} \to \mp \lambda^{\pm} A(X,T) \text{ as } Y \to \infty, \tag{4.5b}$$

in view of (4.3a-c) and its upper-wall counterpart. The solution then has the form of a free interaction [22] in which, for equal $\lambda^{\pm} (= \lambda)$ values, $P^+ = -P^-$ and, using $\bar{p} = 2P^+, \bar{b} = -2\lambda A$ for convenience, the upstream response has

$$\bar{p} = -(J/2\lambda) G \kappa^2 e^{\kappa X}, \bar{b} = G e^{\kappa X} \text{ for } X < 0. \tag{4.6a}$$

The constant G is unknown, while the real positive eigenvalue $\kappa = \left\{-6\,\mathrm{Ai}'(0)/J\right\}^{3/7} \lambda^{5/7}$. The corresponding downstream response is

$$\bar{p} = (J/2\lambda) \left[\bar{\Gamma} \kappa_1^2 \exp(\kappa_1 X) + cc\right], \bar{b} = -[\bar{\Gamma} \exp(\kappa_1 X) + cc] \text{ for } X > 0, \tag{4.6b}$$

with unknown complex constant $\bar{\Gamma}$ along with complex eigenvalues $\kappa_1 = \kappa \exp(6i\pi/7)$ and its complex conjugate (cc). The decaying exponentials above are to ensure negligible influence far upstream and far downstream from the body. On the other hand $\bar{p}, \bar{b}$ must be continuous across $X = 0$, giving values that agree with the Re^{-m} contribution in (2.2), and (4.4) requires $\bar{b} - \bar{b}(0) \sim 2\lambda \beta_{d,u} X$ as $X \to 0\pm$ to accommodate the point discontinuity due to matching with the shorter-scale response of the previous section. The conditions are sufficient to fix the four unknown real constants $G, \bar{\Gamma}_r, \bar{\Gamma}_i$ in addition to β_d, yielding in particular

$$-G\kappa^2 = 2(\bar{\Gamma}\kappa_1^2)_r; G = -2\bar{\Gamma}_r; -2\lambda[\beta_u - \beta_d] = -2(\bar{\Gamma}\kappa_1)_r - G\kappa. \tag{4.6c}$$

Here the subscripts r, i denote real and imaginary parts respectively. Hence we find

$$\left\{(\kappa/\lambda)G, (\kappa/\lambda)\bar{\Gamma}_r, (\kappa/\lambda)\bar{\Gamma}_i, \beta_d\right\} = \{2\cos(\pi/7), -\cos(\pi/7), -\sin(\pi/7), -1\} \frac{\beta_u - \beta_d}{1 + \cos(\pi/7)}, \tag{4.6d}$$

which determines the four coefficients since the difference $[\beta_u - \beta_d]$ is prescribed by the relative-core solutions of § 3. See figure 10. A potentially useful overall result here is

$$\beta_u = -\bar{\mu} \beta_d \tag{4.7}$$

where $\bar{\mu} = \cos(\pi/7) = 0.900969$ (approx.) gives the ratio of the streamline slopes for the short-scale behaviour in (2.10a,b) in the linear range whereas numerical work is required on (4.3a)-(4.4) to give $\bar{\mu}$ for the nonlinear range. A similar result holds for unequal $\lambda^{\pm}$ values.

The determination of temporal growth and body motion. The result (4.7) combines with two inviscid ones in the previous section, namely (3.2a,b) in the form

$$\hat{M} Q^2 (H^* + \frac{1}{2}\beta^*_u L - A^*_u) = C^*_L, \tag{4.8a}$$

$$\hat{I} Q^2 (1 + \beta^*_u) = C^*_M, \text{ with } C^*_M = \int_0^L (x - \frac{1}{2}L) \left\{p^*(x, y_0-) - p^*(x, y_0+)\right\} \mathrm{d}x, \tag{4.8b}$$

to yield the entire body-scale solution, not just the relative version (3.6a-i). Thus the difference D_s (calculated from (3.6a-g) as in earlier figures) when coupled with (4.7) yields

$$\beta^*_u = \bar{\mu} D_s / (1 + \bar{\mu}) \tag{4.9a}$$

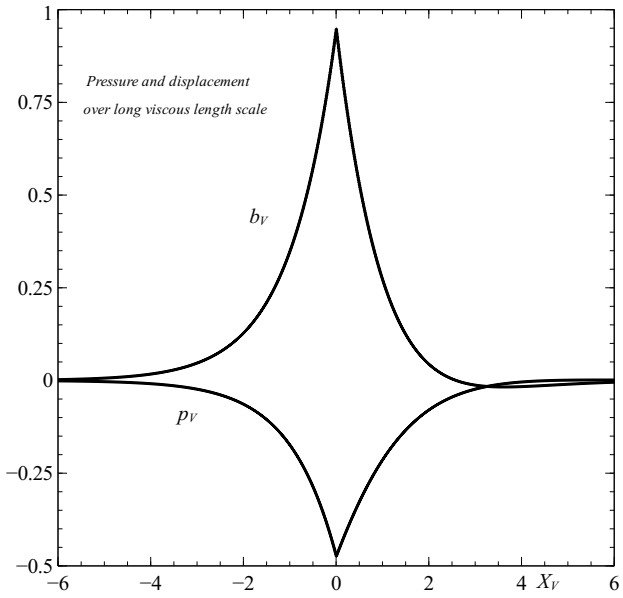

Figure 10. The behaviour over the longer viscous scale, showing scaled pressure and displacement effects $p_V = \bar{p}/(J\kappa B)$, and $b_V = \kappa\bar{b}/(\lambda B)$ as a function of $X_V = \kappa X$, where $B = \beta_u - \beta_d$.

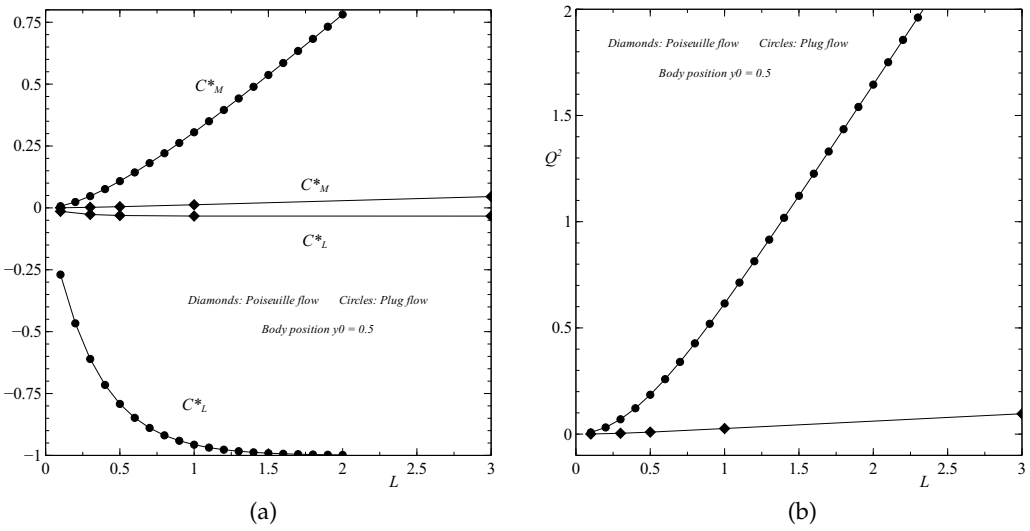

Figure 11. Influence of the body length L on (a) scaled lift and moment, (b) growth factor Q^2 (with $\hat{I}$ normalised to 1), for oncoming Poiseuille and plug flows.

and so (4.8b) yields the temporal power Q explicitly as

$$Q = \pm\{C^*_M(1+\bar{\mu})\hat{I}^{-1}(1+\bar{\mu}+D_s)^{-1}\}^{1/2}. \tag{4.9b}$$

Recall that D_s is proportional to the lift, see (3.6g). It follows that the normalised height $H^* + \frac{1}{2}\beta^*_u L - A^*_u$ is then fixed by (4.8a), after which K_H can be used to give the K^* value. Hence the body motion is determined. See figure 11 which confirms that one root Q is real and positive yielding instability in every case. This is sensible physically as θ being positive induces negative

lift which, through the body motion, then enhances the positivity of θ and so leads to a self-sustaining growth.

Over the $O(1)$ length scale. Distinct viscous effects also arise on the shorter axial scale of (2.1). In the current scenario these are mainly secondary effects as regards body movement and occur mostly in the wall layers. Near the lower wall there are two layers. The thicker one is a continuation of the wall layer in (4.2c) in which $y = Re^{-2/7}Y$,

$$[u,\psi,p] = [Re^{-2/7}U_0 + Re^{-3/7}U_1,\ Re^{-4/7}\Psi_0 + Re^{-5/7}\Psi_1,$$
$$Re^{-4/7}P_0 + Re^{-5/7}P_1 + Re^{-16/21}P_{11}] + \dots \quad (4.10a)$$

and $P_1 = \tilde{\pi}(T)x$. Here the profile U_0 is U evaluated at $X = 0$, where it is continuous, likewise $P_0 = P^-$ at zero X, the function $\tilde{\pi}(T) = U_0''(0,T)$, and $U_0 \sim \lambda^- Y + u_E(0,T)$ at large Y. The contribution U_1 tends to $\lambda^- A^-(x,T)$ at large Y to match with the core of § 2. The core produces a slip velocity $Re^{-2/7}u_E(0,T) + Re^{-3/7}\lambda^- A^-$ due to (2.2); the first term feeds into the layer of (4.10a) while the second term feeds into the layer (4.10b) below. The displacement effect proportional to A^- continues unaltered down through the layer (4.10a). The thinner wall layer then has $y = Re^{-1/3}Y_1$,

$$[u,\psi,p] = \Big[Re^{-1/3}\lambda^- Y_1 + \frac{1}{2}Re^{-8/21}\tilde{\pi}Y_1^2 + Re^{-3/7}U_{11},$$
$$\frac{1}{2}Re^{-2/3}\lambda^- Y_1^2 + (1/6)Re^{-5/7}\tilde{\pi}Y_1^3 + Re^{-16/21}\Psi_{11},$$
$$Re^{-4/7}P_0 + Re^{-5/7}\tilde{\pi}x + Re^{-16/21}P_{11}\Big] + \dots \quad (4.10b)$$

The $\tilde{\pi}$ factors cancel out in the resulting axial-momentum balance to leave the linearised viscous-inviscid equations as in (4.5a,b) with $(\lambda^\pm, Y, U^\pm, \Psi, X, V, P^\pm)$ replaced by $(\lambda^-, Y_1, U_{11}, \Psi_{11}, x, V_{11}, P_{11})$. The boundary conditions impose (4.5b) with the same replacements; in particular $U_{11} \to \lambda^- A^-(x,T)$ as $Y_1 \to \infty$, matching with the thicker wall layer above. There is a similar two-layered response near the upper wall. The scaled local pressure and WSS contributions on each wall then follow from the direct relations [24]

$$P_{11}^\pm(x,T) = -\gamma^\pm \int_{-\infty}^{x} A^\pm(s,T)(x-s)^{-2/3}\,\mathrm{d}s, \quad (4.11a)$$

$$\partial U_{11}^\pm/\partial Y_1(x,0,T) = \delta^\pm \int_{-\infty}^{x} \partial_s A^\pm(s,T)(x-s)^{-1/3}\,\mathrm{d}s, \quad (4.11b)$$

where $\gamma^\pm = -3\,\mathrm{Ai}'(0)(\lambda^\pm)^{5/3}/\Gamma(1/3) = 0.289838(\lambda^\pm)^{5/3}$,

and $\delta^\pm = 3\,\mathrm{Ai}(0)(\lambda^\pm)^{4/3}/\Gamma(2/3) = 0.786552(\lambda^\pm)^{4/3}$,

are positive constants. We remark that the $A^\pm$ functions in (4.11a,b) include the contribution $(A_u - \beta_u x)$ in (2.10a) as well as the relative contributions from (3.6a-g). The parabolic nature of (4.11a,b) on their own in the positive x-direction is noted, although the entire system remains elliptic. The predictions for the pressure and WSS can thus be evaluated once the scaled displacement is determined by the relative-core and viscous solutions as in the previous two sections. See figure 12 (in which PE denotes $-P^\pm/\gamma^\pm$).

5. Influence of body length and location

The responses to changes in body size and position are controlled first by (3.6a-g) as regards a normalised form and second by (4.7)-(4.9b) as regards orientation and temporal behaviour. The latter has a universal format but the former, i.e. (3.6a-g), depends on certain details.

Short bodies. When L is small two distinct length scales operate within the body-scale response (3.6a-g). The first is in an inner zone $(x, y - y_0) \sim L(\xi,\eta)$ surrounding the body. There the

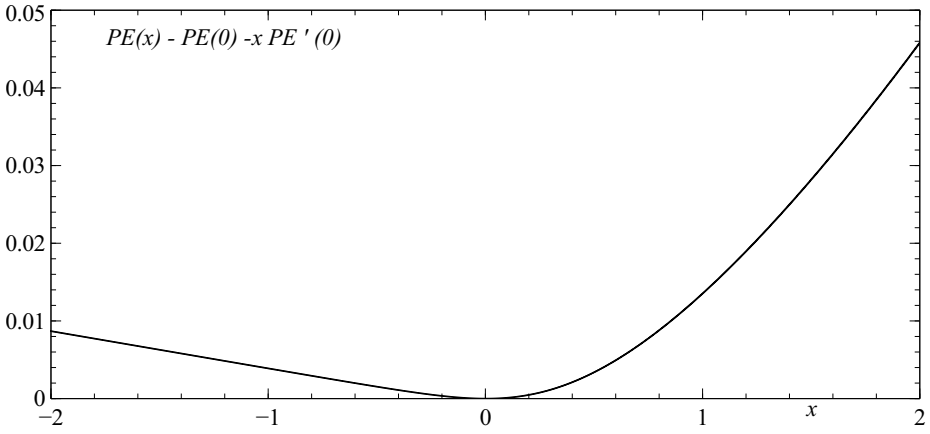

Figure 12. Scaled wall pressure P against x for a representative $A(x)$ on the body scale.

governing equation (3.6a) reduces to Laplace's equation in ξ, η for ψ^* at leading order in L since $u_0(y)$ is approximately $u_0(y_0) + O(L)$ locally. So the local flow is that of an unbounded uniform stream past a thin body at incidence. This satisfies (3.6d,e) but yields a nonzero circulation in which ψ^* is proportional to $C_L^* ln(\xi^2 + \eta^2)$ at large ξ, η.

The second, outer, zone is for (x, y) of $O(1)$ and here the relative problem (3.6a-i) applies in full except that matching with the inner zone requires

$$\psi^* \sim (4\pi)^{-1} C_L^* \ln(x^2 + (y - y_0)^2) \text{ as } (x, y) \to (x, y_0), \tag{5.1}$$

instead of (3.6d,e), and the lift factor C_L^* is known from the inner solution. The approach towards this point-circulation or point-vortex limit problem in the outer zone can be seen in the results of figure 2-4 as L is decreased.

The above is for a general incoming profile $u_0(y)$ such as in (3.7). In the near-plug case (3.8a) however the reduction within the inner zone is exact. For the inner expansion $\psi^* = L\psi_1^* + \ldots$ yields

$$\psi_{1\xi}^* = 1 \text{ on } \eta = 0 \text{ for } 0 < \xi < 1, \tag{5.2a}$$

and an appropriate solution exhibiting symmetry of ψ_1 in η such that

$$\psi_{1\eta}^* = 0 \text{ on } \eta = 0 \text{ for } \xi < 0, \xi > 1, \tag{5.2b}$$

follows. Inverse square root behaviour in the scaled p, u is acceptable at the leading edge $\xi = 0$ but only a square root at the trailing edge $\xi = 1$ by virtue of the Kutta condition. Therefore the complex velocity is

$$u - iv = i(Z - 1)^{1/2}/Z^{1/2} - i \text{ where } Z = \xi + i\eta. \tag{5.2c}$$

This is $O(Z^{-1})$ at infinity, indicating decaying velocities, while along $\eta = 0$ we see the values $u = 0$ for $\xi < 0, \xi > 1$ and $v = 1$ for $0 < \xi < 1$, as required. The scaled complex potential is

$$W_1^* = \phi_1^* + i\psi_1^* = i \int \left[(Z - 1)^{1/2}/Z^{1/2} - 1 \right] dZ + constant; \tag{5.2d}$$

and so $\phi_1^* + i\psi_1 \sim -\frac{1}{2} i \ln(Z)$ at infinity. Thus at infinity a vortex-like effect occurs,

$$\psi_1^* \sim (-\frac{1}{2}) \ln(R), \phi_1^* \sim \frac{1}{2} \tan^{-1}(\eta/\xi), circ \to \pi, \text{ with } R^2 = \xi^2 + \eta^2, \tag{5.2e}$$

which provides the matching condition mentioned just above; $circ$ denotes the scaled circulation. The outer expansion $\psi^* = L \ln(L) + L\psi_2^* + \ldots$ then gives Laplace's equation again but subject to

$$\psi_2^* \sim (-\frac{1}{2})\ln(r) \text{ as } r = \{x^2 + (y-y_0)^2\}^{1/2} \to 0. \tag{5.3a}$$

This corresponds to the point-vortex effect at $(0, y_0)$. The whole channel interior is now mapped to the upper half plane in $\tilde{\tilde{z}} = \exp(\pi z)$ similarly to (3.9a) but such that the upper and lower walls are respectively at $\tilde{\tilde{x}} < 0$ and $\tilde{\tilde{x}} > 0$ along $\tilde{\tilde{y}} = 0$. The small body is at $\tilde{\tilde{z}} = \tilde{\tilde{z}}_0 = \exp(\pi i y_0)$. For the earlier example $y_0 = \frac{1}{2}$ with the body midway across the channel $\tilde{\tilde{z}}_0 = i$. Addition of the image at $\tilde{\tilde{z}} = -i$ and use of symmetry then shows the scaled complex potential to be

$$W_2^* + constant = (-\frac{1}{2})i \ln\left[(\tilde{\tilde{z}} - i)(\tilde{\tilde{z}} + i)\right] = (-\frac{1}{2})i \ln\left[e^{2\pi z} + 1\right], \tag{5.3b}$$

to satisfy (3.8b). In particular along $\hat{y} = 0, \varphi_2^* = 0, \psi_2^* = (-\frac{1}{2})\ln\left[e^{2\pi x} + 1\right]$, which yields the downwash

$$\psi_2^* \sim -\pi x \text{ as } x \to \infty \text{ downstream, whereas } \psi_2^* \to 0 \text{ as } x \to -\infty \text{ upstream.} \tag{5.3c}$$

We may also add $i(A + Bz)$ to (5.3c) with A, B real constants to allow for condition (2.10a) upstream. The result (5.3d) is in keeping with (2.10c) since here $C_L^* = \pi L$ to leading order (see also (3.10d)) and (3.8a) holds.

Long bodies. When L is large, the body-scale response on the $O(1)$ length scale in x (zone 1 say) remains as in (3.6a-g) to leading order except that the conditions (3.6f,g) are not met directly since the trailing edge is far downstream. Instead at large positive x the pressure p decays exponentially and ψ^* approaches $-u_0(y)x$. Far downstream the $O(L)$ length scale (zone 2) then enters play with $x = Lx_3, \psi^* = L\psi_3^* + \ldots$, so that the x derivatives in (3.6a) become negligible and $\psi_3^* = -u_0(y_0)x_3$ at $y = y_0 \pm$ from (3.6d) while (3.6b,c,e,f,g) mostly remain intact. The solution is

$$\psi_3^* = -u_0(y)x_3 \tag{5.4}$$

at leading order. This also satisfies the Kutta condition (3.6e) at $x_3 = 1$ since the pressure is exponentially small; the trailing streamline here just continues at the same incidence as the thin body. The form (5.4) then carries on for all $x_3 > 1$, yielding the required slope condition (3.6g) at large x_3. This slope effect emergent in zone 2 and the dominant scaled lift which is determined entirely by zone 1 are related in the same way as in (3.6h). The near-plug behaviour (3.8a)-(3.10d) also supports the large-L structure above. Thus for zone 1 at leading order (3.10a-c) give the normalised form

$$\psi^* = -\pi^{-1}\cosh^{-1}(e^{-\pi x}) - x + \pi^{-1}ln(2) \text{ for } x < 0; -x + \pi^{-1}ln(2) \text{ for } x > 0, \tag{5.5a}$$

$$p^* = -(e^{2\pi x} - 1)^{-1/2} \text{ for } x > 0, \tag{5.5b}$$

$$C_L^* = -1, \tag{5.5c}$$

along $y = 1/2$. For zone 2 we have the velocity $\sim 1 + O(\exp)$ from (3.10a), which ties in with (5.4) in terms of ψ^*. The asymptotes agree with the trends of the computational findings, for example in terms of the lift in (5.5c) compared with figure 9 and the value $\pi^{-1}\ln(2)$ of ψ^* at the leading edge compared with that in figure 9.

Positioning. If the body is close to one of the walls, say y_0 is small, then we have a small-daughter case [21]. Again two axial length scales govern the response. One is $O(y_0)$ surrounding the leading edge where in scaled form the system (3.6a-i) applies but with $u_0(y)$ replaced by $\lambda^- y$, with 0, 1 in (3.6b) replaced by $0, \infty$, with$K_H - (x - L/2)$ replaced by $k_H - x$ for all $x > 0 (k_H$ unknown) and with (3.6f) abandoned downstream. The solution here is essentially that for uniform vorticity in [21] and shows the pressure decaying exponentially downstream in the small gap and algebraically in sink-like fashion in the rest of the far field, such that the main lift factor C_L^* is created in this $O(y_0)$ zone. The other axial length scale is $O(1)$ where the smaller gap produces negligible pressure throughout and the larger gap flow is forced solely by the sink-like effect at the origin. Far downstream on this scale the trend (3.6f,g) emerges. See figures 6, 7.

6. Further discussion

The study has shown instability occurring at low amplitudes of body thickness and incidence due to fluid-body interaction in the channel. The presence of the finite free body is vital in this self-sustaining response, in particular producing the streamline-slope ratio $\cos(\pi/7)$ during the whole evolution. Nonlinear interactions at increased amplitudes, where the slope ratio alters and the decomposition $\exp(QT)$ no longer applies throughout, are expected to yield significant growth also. Compared with a constriction (which is in essence a body at the wall) of similar length comparable with the channel width, the free body in the core of the flow causes a surprising viscous response involving interaction of two axial scales, one that of the body and the other a long viscous scale. This response in turn is brought about by an effective point discontinuity over the longer scale and a direct connection between body lift and far-field directions in the body-scale problem which, due to the no-slip incident profile, is quite distinct from the classical problem of an airfoil in a wind tunnel.

The evolution that leads to instability here lies in an unconventional range. There is an analogy with the direct simulations in [19] where a delay in relaminarisation is observed when particles are present. The time scale in our case is such that the flow behaviour is quasi-steady, unlike the body motion. Self-consistency then requires the density ratio ρ_{BD}/ρ_D (density of the body over that of the fluid) to exceed the order of $Re^{6/7}$ where Re is a Reynolds number based on the channel width. If we take a typical Re range of interest about 20-100 then ρ_{BD}/ρ_D has to be greater than about 13-50. For water as the fluid few elements satisfy the above restriction but for air many do. Faster evolution would lead to a time derivative first appearing in the longer-scale wall layers of § 5 which would then yield conventional channel-flow instability. Nonlinear effects first emerge in those layers as well, arising from continuation of the exponential instability and making quasi-steady separation a possibility [22]. Increased axial velocity of the body as in Appendix A first has significant effect in the body-scale wall layers where the wall-pressure variation is gradually altered from an integrated form to a form directly proportional to the local displacement.

Other body lengths lead to distinct interactions as inferred from the properties found (§ 5) for a decreased or increased length factor. The former leads to a point-vortex effect while the latter produces a focussed leading-edge effect with little further variation downstream, both indicating substantial changes in interactive structure. Tiny bodies of $O(1)$ aspect ratio are expected to induce circulation as if at a point within the core flow. Other lateral positions of the body likewise herald structural change as the body approaches the wall-layer scale, pressure and lift become concentrated near the leading edge and the wake direction becomes identical with the body direction at the trailing edge. Faster downstream axial movement of the body producing a switch in the wall response towards that of a classical boundary layer with the influence of basic shear diminished acts as a springboard for modelling of a much wider parameter range. Inflectional and critical-layer properties may then come into play. The body could even travel upstream against the flow, implying yet another form of instability, or [18] lie within the viscous wall layer as part of touchdown upon or lift off from the wall.

It would be helpful to compare the theory quantitatively with experiments or direct numerical simulations on finite bodies or both. None of relevance to the present basic problem have been found yet. It may be that instead the modelling should move on to examine many bodies [17], either of finite size as here or tiny (where solutions can be superposed) to seek further connections with studies such as [19]. A qualitative connection exists in terms of instability and relaminarisation as mentioned earlier, and understanding of the length scales as in figure 1 is clearly of importance. Meanwhile the potential application to boundary layers and three-dimensional interactions is noted. Both three-dimensionality and the flow separation mentioned above occur in many of the applications described in the introduction and these important aspects still require considerable study.

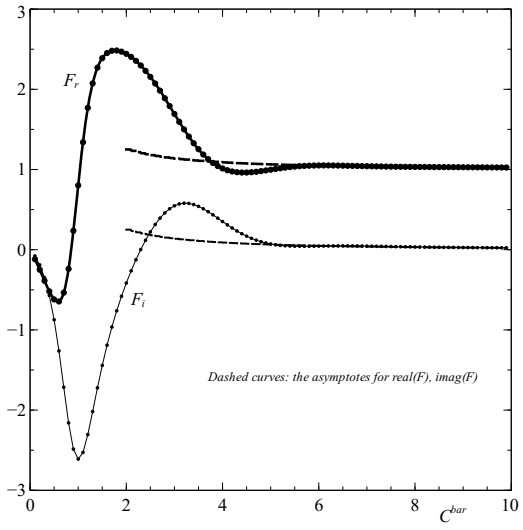

Figure 13. The real and imaginary parts of the Tietjens function F plotted against $\bar{C}\left\{=C\alpha^{1/3}/(\lambda^{\pm})^{2/3}\right\}$. Asymptotes for large $\bar{C}$ are shown as dashed curves.

A. Effect of increased axial velocity of the body

The free-body movement in the axial direction first becomes significant when $c_{\rm body}$ is increased to the order $Re^{-1/3}$, say $Re^{-1/3}C$. This is then a primary effect in the viscous wall layers over the body scale. It remains secondary in the Blasius-like layers on the divider, in the structure over the $O(Re^{-1/7})$ axial scale and elsewhere.

In the lower viscous layer (4.10b) the scaled velocity $\lambda^- Y_1$ now becomes $\lambda^- Y_1 - C$ and similarly in the governing equations (4.5a,b) modified as described just after (4.10b). Taking a Fourier transform axially with transformed variable α converts (4.5a-c) to Airy's equation for the transformed shear stress,

$$(\lambda^- Y - C)i\alpha\tau^{-(F)} = \tau_{YY}^{-(F)}(\text{ where } \tau^- = U_Y^-), \tag{A 1}$$

[25] with $^{(F)}$ denoting the Fourier transform and Y standing for Y_1. We then apply the boundary conditions on $\tau_Y^{-(F)}$ at $Y = 0$ and on the integral of $\tau^{-(F)}$ with respect to Y from 0 to ∞ to obtain the pressure-transform and WSS-transform solutions

$$P^{-(F)}(\alpha, T) = C\lambda^- A^{-(F)}(\alpha, T)/F(\alpha), \tag{A 2}$$

$$\tau^{-(F)}(\alpha, 0, T) = (i\alpha)^{2/3}/(\lambda^-)^{1/3} P^{-(F)}(\alpha, T)\,\mathrm{Ai}(\xi_0)/\,\mathrm{Ai}'(\xi_0), \tag{A 3}$$

$$F(\alpha) = -\xi_0 \int_{\xi_0}^{\infty} \mathrm{Ai}(\xi) d\xi/\,\mathrm{Ai}'(\xi_0), \tag{A 4}$$

and the constant $\xi_0 = -C(i\alpha)^{1/3}(\lambda^-)^{-2/3}$. Here F is the Tietjens function [26,27]; see figure 13. The forms (A2), (A3) allow the pressure and WSS responses to be expressed explicitly in terms of the displacement effect, or vice versa, as the responses develop in time.

For small C with α, λ^- of $O(1)$ the results (A2)-(A3) retrieve (4.11a,b) on inversion. For large C with α, λ^- of $O(1)$ on the other hand we obtain

$$P^-(x, T) = C\lambda^- A^-(x, T), \tag{A 5}$$

for the pressure at leading order. This stems from the asymptotes in figure 13 and agrees with the wall layer becoming a classical boundary layer in effect since $\lambda^- Y$ in (A1) then becomes negligible as Y scales with $C^{-1/2}$. The point-by-point result (A5) contrasts with the integral result (4.11a).

References

1. Marxen, M., Sled, J. G., Yu, L. X., Paget, C. and Henkelman, R. M. Comparing microsphere deposition and flow modelling in 3D vascular trees. *Am J Physiol Heart Circ Physiol*, 291, H2136-2141. 2006.
2. Sinclair, M., Lee, J., Schuster, A., Chiribi, A., van den Wijngaard, J., van Horssen, P., Siebes, M., Spaan, J. A. E., Nagel, E. and Smith, N. P. Microsphere skimming in the porcine coronary arteries: implications for flow quantification. *Res, 100*, 59-70. 2015.
3. Uspal, W. E., Popescu, M. N., Dietrich, S. and Tasinkevych, M. Self-propulsion of a catalytically active particle near a planar wall: from reflection to sliding and hovering. *Soft Matter*, 11, 434-438. 2015.
4. Lee, T-R., Choi, M., Kopacz, A. M., Yun, S-H., Liu, W. K. and Decuzzi, P. On the near-wall accumulation of injectable particles in the microcirculation: smaller is not better. *Sci Repts*, 3:2079, 1-8. 2013.
5. AGARD Ice accretion simulation. Report of the fluid dynamics working group 20. *AGARD Advisory Report*, AGARDAR-344, ISBN 92-836-1067-9. 1997.
6. Gent, R. W., Dart, N. P. and Cansdale, J. T. Aircraft Icing. *Phil Trans Roy Soc, A* 358, 2873âĂŞ2911. 2000.
7. Vreman, A. W. Turbulence attenuation in particle-laden flow in smooth and rough channels. *J Fluid Mech*, 773, 103-136. 2015.
8. Smith, F. T. and Wilson, P. L. Fluid-body interactions: clashing, skimming, bouncing. *Phil Trans A Roy Soc, A* 369, 3007-3024. 2011.
9. Gavze, E. and Shapiro, M. Particles in a shear flow near a solid wall: effect of nonsphericity on forces and velocities. *Int J Multiphase Flow*, 23, 155-182. 1997.
10. Sugihara-Seki, M. The motion of an ellipsoid in tube flow at low Reynolds number. *J Fluid Mech*, 324, 287-308. 1996.
11. Meis, M., Varas, F., Velazquez, A. and Vega, J. M. Heat transfer enhancement in micro-channels caused by vortex promoters. *Int J Heat and Mass Transfer*, 53, 29-40. 2010.
12. Mettu, S., Verma, N. and Chhabra, R. P. Momentum and heat transfer from an asymmetrically confined circular cylinder in a plane channel. *Heat and Mass Transfer*, 42, 1037-1048. 2006.
13. Sahin, M. and Owens, R. G. A numerical investigation of wall effects up to high blockage ratios on two-dimensional flow past a confined circular cylinder. *Phys Fluids*, 16, 1305-1320. 2004.
14. Kumar, B. and Mittal, S. Effect of blockage on critical parameters for flow past a circular cylinder. *Int J Num Meth Fluids*, 50, 987-1001. 2006.
15. Rehimi, F., Aloui, F., Nasrallah, S. B., Doubliez, L. and Legrand, J. Experimental investigation of a confined flow downstream of a circular cylinder centred between two parallel walls. *J Fluids and Structures*, 24, 855-882. 2008.
16. Kidanemariam, A. G., Chan-Braun, C., Doychev, T. and Uhlmann, M. Direct numerical simulation of horizontal open channel flow with finite-size, heavy particles at low solid volume fraction. *New J Phys*, 15 (2), 025031. 2013.
17. Smith, F. T. and Ellis, A. S. On interaction between falling bodies and the surrounding fluid. *Mathematika*, 56, 140-168. 2010.
18. Wilson, P. L. and Smith, F. T. Body-rock or lift-off in flow. *J Fluid Mech*, 735, 91-119. 2013.
19. Loisel, V., Abbas, M., Masbernat, O. and Climent, E. The effect of neutrally buoyant finite-size particles on channel flows in the laminar-turbulent transition regime. *Phys Fluids, 25 (no 12)*. ISSN 1070-6631. 2013.
20. Smith, F. T. The separating flow through a severely constricted symmetric tube. *J Fluid Mech*, 90, 725-754. 1979.
21. Smith, F. T. and Jones, M. A. One-to-few and one-to-many branching tube flows. *J Fluid Mech*, 423, 1-31. 2003.
22. Smith, F. T. Upstream interactions in channel flows. *J Fluid Mech*, 79, 631 655. 1977.
23. Ovenden, N. C., Smith, F. T. and Wu, G-X. The effects of nonsymmetry in a branching flow network. *J Eng Math*, 63, 213-239. 2009.
24. Pruessner, L. and Smith, F. T. Enhanced effects from tiny flexible in-wall blips and shear flow. *J Fluid Mech*, 772, 16-41. 2015.
25. Stewartson, K. On laminar boundary layers near corners. *Quart J Mech Applied Math*, 23, 137-152. 1970.
26. Miles, J. W. The hydrodynamic stability of a thin film of liquid in uniform shearing motion. *J Fluid Mech*, 8, 593-610. 1960.

27. Smith, F. T. On the non parallel flow stability of the Blasius boundary layer. *Proc Roy Soc, A* 366, 91-109. 1979.